GENERALIZED WAVE PROPAGATION PROBLEMS AND DISCRETE EXTERIOR CALCULUS

JUKKA RÄBINÄ, LAURI KETTUNEN, SANNA MÖNKÖLÄ, AND TUOMO ROSSI

Abstract. We introduce a general class of second-order boundary value problems unifying application areas such as acoustics, electromagnetism, elastodynamics, quantum mechanics, and so on, into a single framework. This also enables us to solve wave propagation problems very efficiently with a single software system. The solution method precisely follows the conservation laws in finite-dimensional systems, whereas the constitutive relations are imposed approximately. We employ discrete exterior calculus for the spatial discretization, use natural crystal structures for three-dimensional meshing, and derive a "discrete Hodge" adapted to harmonic wave. The numerical experiments indicate that the cumulative pollution error can be practically eliminated in the case of harmonic wave problems. The restrictions following from the CFL condition can be bypassed with a local time-stepping scheme. The computational savings are at least one order of magnitude.

1. Introduction

We present a unifying class of wave propagation problems and a framework to solve such problems in finite dimensional spaces. The key properties of the numerical solutions are the exact agreement with conservation laws, approximate constitutive relations, and explicit solution processes. The class of wave propagation problems covers both the classical and modern fields of physics, such as electromagnetism, sound propagation, elastic waves, quantum mechanics, and so on.

The class of wave propagation problems we deal with is characterized by a partial differential equation system:

$$\partial_t(\mathrm{M}u) + \mathrm{D}u = f + \mathrm{F}u, \tag{1}$$

where ∂_t is the time differential, M is a positive definite operator, D is the differential (a skew self-adjoint operator), and u is a formal sum of the scalar and vector fields representing the propagating wave. Function f is a source term, and Fu represents the power into and out of the system.

Date: February 15, 2018.

2010 *Mathematics Subject Classification.* Primary 35L65, 58A10, 58A14, 58J32, 58J90; Secondary 65M06, 65M12, 65M22.

Key words and phrases. Differential geometry, exterior algebra, boundary value problems, acoustics, electromagnetism, elasticity, quantum mechanics, finite difference, discrete exterior calculus.

The computations presented were performed using the computing resources provided by the CSC — IT center for science, owned by the Finnish Ministry of Education and Culture. The research was supported by the ERC Advanced Grant project SAEMPL (No. 320733). We also acknoledge the anonymous referees for valuable comments, which significantly improved the presentation of the paper.

In $(3+1)$-dimensions and in terms of classical vector analysis, operators M and D are given by

$$\mathrm{M} = \begin{pmatrix} \mathrm{m}_0 & & & \\ & \mathrm{m}_1 & & \\ & & \mathrm{m}_2 & \\ & & & \mathrm{m}_3 \end{pmatrix}, \quad \mathrm{D} = \begin{pmatrix} & \mathrm{div} & & \\ \mathrm{grad} & & -\mathrm{curl} & \\ & \mathrm{curl} & & -\mathrm{grad} \\ & & -\mathrm{div} & \end{pmatrix},$$

where $\mathrm{m}_0, \ldots, \mathrm{m}_3$ are scalars. The corresponding formal sum u is then given by $u = (u_0, u_1, u_2, u_3)^T$, where u_0 and u_3 are scalar fields and u_1 and u_2 are vector fields. Consequently, the first column of M and of D operate on scalar field u_0, the second one on vector field u_1, and so on.

Many wave propagation problems in physics can now be given as instances of (1) by selecting some of the entries in the formal sum u as null (see Table 1; more examples with further details are shown in Section 5.)

choice of formal sum u	branch of physics
$(u_0, u_1, 0, 0)^T$ or $(0, 0, u_3, u_4)^T$	acoustics
$(0, u_1, u_2, 0)^T$	electromagnetism
$(u_0, u_1, u_2, 0)^T$ or $(0, u_1, u_2, u_3)^T$	elastodynamics
$(u_0, u_1, u_2, u_3)^T$	quantum mechanics

TABLE 1. The correspondence between the choices of u and different field theories in three dimensions.

This class of wave propagation problems is characterized by some common properties. Especially, the multiplication of the homogeneous form of Eq. (1) from left by the adjoint u^* implies $0 = u^*\partial_t(\mathrm{M}u) + u^*\mathrm{D}u = \frac{1}{2}\partial_t(u^*\mathrm{M}u)$. This is about the conservation of scalar function $u^*\mathrm{M}u$, which can be interpreted in many cases as energy conservation.

This framework coincides with R. Picard's "Mother PDE" suggesting a setting from which a large class of linear partial differential equations can be inherited [29]. His work offers proofs for the well-posedness, existence, and uniqueness of solutions.

Our spatial discretization strategy is an extension of generalized Yee-like schemes; that is, finite difference time domain (FDTD) techniques [51, 37]. Such approaches are also referred to as the finite integration technique (FIT) [49] or the cell method [41, 43, 42].

The discretization process relies on the work presented in [6, 7] recognizing the differentiable and metric structure. The generalized Yee-like schemes are nowadays known by the name *discrete exterior calculus* (DEC), thanks to the intuitive correspondence between the "continuous" and "discrete" models [21, 16, 35]. This is to say, the counterparts of the differential operators and the so-called *Hodge operator* are matrices in finite-dimensional spaces. The matrices representing the differential operators do not depend on the metric, and hence, they can be recognized as finite-dimensional counterparts of the so-called *exterior derivative*.

In this paper, we primarily examine time integration schemes, tiling strategies of space, and approximations of the Hodge operator, which are all critical in coming up with efficient solution methods. This study generalizes our previous work specialized in electromagnetism [31, 32].

2. Spatial discretization

The cornerstone of spatial discretization is the *Stokes theorem*; the exterior derivative $\mathrm{d}w$ of a differential form w integrated over an orientable manifold Ω should coincide with the integral of w over the boundary $\partial\Omega$. That is,

$$\int_{\Omega} \mathrm{d}w = \int_{\partial\Omega} w. \tag{2}$$

To construct a system of equations whose solution approximates the wave problem, first a finite-dimensional approximation of function u in Eq. (1) is generated with a linear combination of basis functions. That is, the approximation of u is $\sum_i \bar{u}_i w_i$, where column vector $\bar{u}$ is the finite-dimensional solution and the w_i's form the set of basis functions. In particular, if $\bar{u}$ and the basis functions are chosen such that coefficients $\bar{u}$ correspond with the values of functions at vertices, circulations along edges, fluxes on faces, and with net masses in volumes, and then the finite-dimensional counterparts of the exterior derivative d and correspondingly of its metric counterparts grad, curl, and div are obtained by imposing Eq. (2) to hold on all edges, faces, and volumes of the finite element mesh.

In more detail, let us call the sets of p-**cells** of an n-dimensional finite element kind of mesh by $\mathcal{C}_p$, $p = 0, \ldots, n$. In addition, let us assume that each set is indexed by integers and the p-cells $c_j^p \in \mathcal{C}_p$ are oriented.

The formal sums $\sum_j \alpha_j^p c_j^p$, where $\alpha_j^p \in \mathbb{R}$, are called p-**chains** [50]. The boundary of a $(p+1)$-chain is a p-chain:

$$\sum_j \alpha_j^p c_j^p \;=\; \partial \left(\sum_i \alpha_i^{p+1} c_i^{p+1} \right) .$$

We are particularly interested in the chains whose real number coefficients α are either ± 1 or 0. These are the chains that are assemblies of the cells of the finite element mesh. Consequently, hereinafter we assume $\alpha_j^p \in \{-1, 0, 1\}$.

The incidence relations between the cells of the finite element mesh can be expressed with so-called incidence matrices. Let $\mathbf{d}_p$ be a matrix such that entry $\mathbf{d}_p(i,j) = 0$ if cell c_j^p is not on the boundary of cell c_i^{p+1}, $\mathbf{d}_p(i,j) = 1$ if cell c_j^p is on the boundary of cell c_i^{p+1} and their orientations match, and $\mathbf{d}_p(i,j) = -1$ if cell c_j^p is on the boundary of cell c_i^{p+1} but their orientations do not match. This implies that the boundary of a $(p+1)$-chain can now be given by

$$\partial \left(\sum_i \alpha_i^{p+1} c_i^{p+1} \right) \;=\; \sum_{i,j} \alpha_i^{p+1} \mathbf{d}_p(i,j)\, c_j^p \,.$$

This is to say that $\mathbf{d}_p$ can be interpreted as the discrete counterpart of boundary operator ∂.

A p-**cochain** maps p-chains to real numbers. Accordingly, the integral of field u on the p-manifold corresponding with p-chain $\sum_j \alpha_j^p c_j^p$ can be understood as a p-cochain $\sum_j \alpha_j^p \bar{u}_p(j)$ where $\bar{u}_p(j) = \int_{c_j^p} u$.

The Stokes law implies the derivative of p-cochain can now be given by

$$\sum_{i,j} \alpha_i^{p+1} \mathbf{d}_p(i,j)\, \bar{u}_p(j) \,,$$

and consequently, in DEC one calls $\mathbf{d}_p$ the **discrete exterior operator** and considers $\bar{u}_p$ as a **discrete** p**-form**. (Be aware, however, they are only finite-dimensional counterparts to the exterior derivative d and differential forms.) In a three-dimensional metric space, $\mathbf{d}_0$, $\mathbf{d}_1$, and $\mathbf{d}_2$ also correspond to the operators grad, curl, and div, respectively.

Wave propagation problems contain two partial differential equations. In the DEC approach, a dual pair of a finite element kind of mesh is exploited, one to each differential equation. Namely, the two meshes are called the **primal** and **dual** meshes. On the discrete level, the skew-symmetric property of D in Eq. (1) is obtained by associating each p-cell c_j^p of the primal mesh with the $(n-p)$-cell c_j^{p*} of the dual mesh. Then the discrete exterior operator in the dual mesh becomes $\mathbf{d}_p^T$; that is, the transpose of $\mathbf{d}_p$ (see Table 2).

on primal mesh	counterpart	on dual mesh	counterpart
$\mathbf{d}_0$	grad	$\mathbf{d}_0^T$	$-$div
$\mathbf{d}_1$	curl	$\mathbf{d}_1^T$	curl
$\mathbf{d}_2$	$-$div	$\mathbf{d}_2^T$	grad

TABLE 2. The correspondence between discrete exterior derivatives and metric-dependent operators.

In addition to the differential equations, wave problems incorporate material laws, which hold at each ordinary point of the domain, and hence they are local conditions. In the continuous model, the material laws are in composition with the Hodge operator. In the linear case, they can be incorporated into the Hodge relation. Consequently, in DEC, the material laws are typically included in the **discrete Hodge** operator mapping primal p-chains onto dual $(n-p)$-chains [21, 16, 35]. Accordingly, the quality of meshes plays a major role in the material approximation.

It is desirable that the meshes are interlocked such that the corresponding (supports of) primal and dual cells intersect near their centers. We would like to emphasize that the cells having common points is not a necessary condition. To end up with a diagonal discrete Hodge matrix, it is enough to assume the primal and dual cells are perpendicular to each other. The *Delaunay-Voronoi duality* is a well-known example of such a pair of interlocked meshes [47, 14, 1, 27].

Once a pair of dual meshes exists, the following step is to impose the material laws. Let the discrete primal p-forms and dual $(n-p)$-forms be denoted by $\bar{u}_p$ and $\bar{u}_{p*}$, respectively. In the discrete case, the material law is of the form $\bar{u}_{p*} = \star_p \bar{u}_p$, where $\star_p$ is a discrete Hodge star. When the mesh grain tends to zero, the so-called consistency error [7] should vanish. This is achieved if the entries of the discrete Hodge are chosen such that

$$\star_p(j,j) = \frac{\int_{c_j^{p*}} u}{\int_{c_j^p} u} = \frac{|c_j^{p*}|}{|c_j^p|}. \tag{3}$$

We call this matrix as a **general Hodge approximation**.

To sum up, the finite-dimensional counterpart of Eq. (1) is now given by

$$\partial_t(\mathbf{M}\bar{u}) + \mathbf{D}\bar{u} = \bar{f} + \mathbf{F}\bar{u}, \tag{4}$$

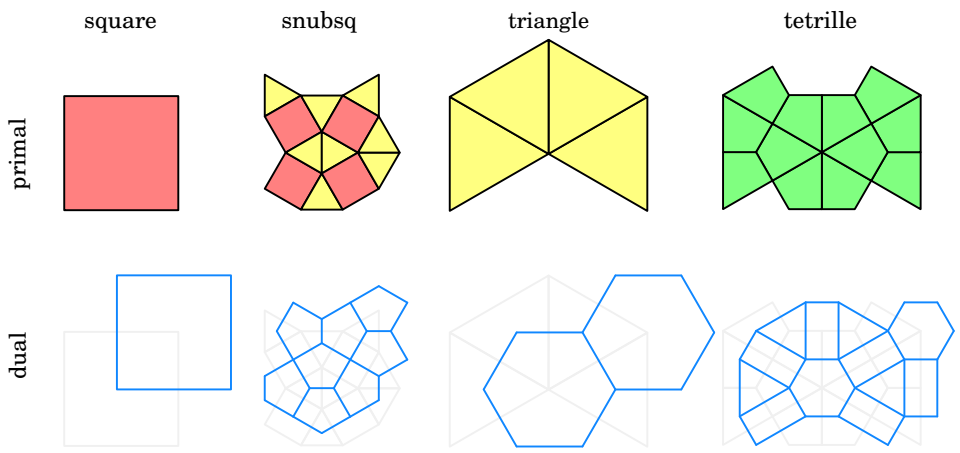

FIGURE 1. The primal and dual cells of repetitive two-dimensional tilings.

where $\mathbf{M}$ is a diagonal positive definite matrix and $\mathbf{D}$ is a skew-symmetric matrix given by

$$\mathbf{M} = \begin{pmatrix} \star_0\mathbf{m}_0 & & & \\ & \star_1\mathbf{m}_1 & & \\ & & \star_2\mathbf{m}_2 & \\ & & & \star_3\mathbf{m}_3 \end{pmatrix}, \quad \mathbf{D} = \begin{pmatrix} & -\mathbf{d}_0^T\star_1 & & \\ \star_1\mathbf{d}_0 & & -\mathbf{d}_1^T\star_2 & \\ & \star_2\mathbf{d}_1 & & -\mathbf{d}_2^T\star_3 \\ & & \star_3\mathbf{d}_2 & \end{pmatrix}.$$

Column vectors $\bar{f}$ and $\mathbf{F}\bar{u}$ represent the source terms and power transfer in the finite-dimensional case.

2.1. **Structured Voronoi-Delaunay grids.** The Voronoi-Delaunay mesh generation starts from establishing the primal nodes. For a given set of nodes, one calculates a Voronoi-diagram using a metric in which the material parameters are isotropic. The cells of the Voronoi-diagram indicate the partitioning for the dual mesh. The p-cells of the primal mesh are determined by associating them with the corresponding $(n-p)$-cells of the dual mesh. Both primal and dual meshes can include simplicial and non-simplicial cells. The intersections of (supports of) primal and dual cells locate at the circumcenters of each primal cells.

The Voronoi-Delaunay process enables both structured and unstructured mesh generation. This paper considers mainly structured grids consisting of homogeneous blocks. The main advantage of such grids is that the duplication process makes the mesh generation fast and also suitable for parallel computing. Due to recurring elements, the disadvantages are that the grids hardly adapt for curved and oblique interfaces, and the local adjustment of element density can be difficult. To overcome this, the different structured grids can be merged together such that unstructured elements exist only at transition layers. In finite difference approaches, the Cartesian grids imply non-identical wave propagation speeds in different directions. We consider alternative structured tilings to eliminate this property.

In two dimensions, we select four different tilings, as illustrated in Fig. 1. The first two tilings, the square and the snub square, are periodic by a 90 degrees increment, while the last two, the triange and the tetrille (also known as deltoidal trihexagonal tiling [11]), are periodic by a 60 degree increment. The edges of the

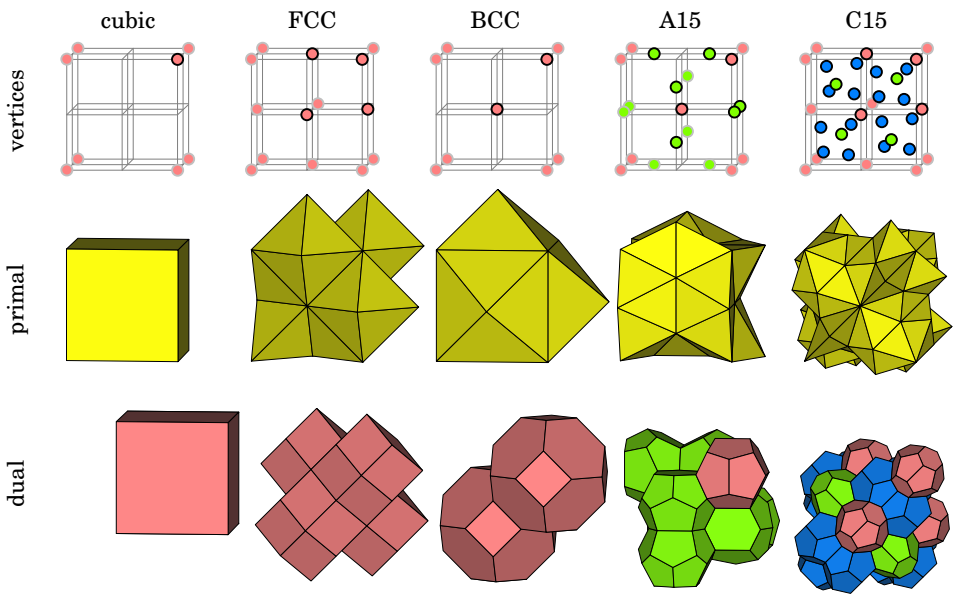

FIGURE 2. The vertex positions and the resulting primal and dual cells in three-dimensional tilings.

square and the triangle tiling have only two and three orientations, respectively. Both the snub square and the tetrille have six different edge orientations, and thus, we anticipate better matches in propagation speeds in different directions.

In three dimensions, we consider five different tilings based on a cubic lattice (see Fig. 2). The space can be tiled by such blocks. Thus, the implementation for these structures is, in principle, as simple as for a primitive cubic structure. A finite difference scheme with the cubic tiling corresponds to the conventional Yee scheme [51].

The face-centered cubic (FCC) and the body-centered cubic (BCC) are the main structures in cubic crystal systems [12]. They are constructed from a cubic grid by adding a vertex at each face or body center, respectively. The FCC tiling is composed of alternating regular octahedra and regular tetrahedra at a ratio of 1:2. The dual body elements are Kepler's rhombic dodecahedra consisting of 12 congruent rhombic faces [24]. The primal of the BCC grid is composed of congruent tetrahedra, where each face is a congruent isosceles triangle. The dual tiling consists of truncated octahedra, each having six square faces and eight regular hexagon faces. This tessellation is known as the Kelvin structure, first introduced in [40]. Due to its sharp dihedral angles, the BCC grid is preferred when a finite difference scheme is applied on tetrahedral meshes [5, 46].

To obtain sharper dihedral angles, we recall the concept of tetrahedrally close-packed (TCP) structures described by Frank and Kasper [20]. Mainly, we consider the A15 and the C15 structures, where the vertex sets are based on the BCC and the FCC, respectively. The maximum dihedral angles of TCP structures are relatively sharp compared to the BCC structure, and the smallest maximal angle of 74.20 degrees is achieved by C15 [19]. The dual elements of TCP structures are theoretically of good quality, since they include only pentagonal and hexagonal faces, with no

adjacent hexagons [36]. Besides, the dual structure of A15 was found to be a counterexample to Kelvin's conjecture on minimal surfaces [48]. In modern knowledge, this so-called Weaire-Phelan structure partitions a three-dimensional space into cells of equal volume with the smallest area of surface between them [25, 18, 34]. The previous studies indicated relatively isotropic properties when a finite difference scheme was applied with TCP structures in the application area of electromagnetism [32].

3. Time integration

The solution of Eq. (4) is about time integration. For this, $\bar{u}$ and $\bar{f}$ are considered as indexed families of column vectors and the k:th instances are denoted by $\mathbf{u}^k$ and $\mathbf{f}^k$, respectively. The time differential $\partial_t \bar{u}$ is approximated with central difference $\frac{\mathbf{u}^{k+1}-\mathbf{u}^{k-1}}{\sigma}$, where $\sigma = 2\Delta t$, and Δt is the time step size between instances. The time integration procedure for Eq. (4) becomes

$$\sigma^{-1}\mathbf{M}(\mathbf{u}^{k+1} - \mathbf{u}^{k-1}) + \mathbf{D}\mathbf{u}^k = \mathbf{f}^k + \mathbf{F}\mathbf{u}^k. \tag{5}$$

Multiplication from left by $\mathbf{M}^{-1}\sigma$ leads to solution process, where the instance $\mathbf{u}^{k+1}$ is calculated from two previous instances $\mathbf{u}^k$ and $\mathbf{u}^{k-1}$. Thus, the time integration method is explicit. If $\mathbf{M}$ is diagonal, then this yields a highly efficient solution method.

In the so-called leapfrog time-stepping procedure, the discrete 0- and 2-forms are differentiated at even time instances and the discrete 1- and 3-forms at the odd ones. Accordingly, for an even k we write

$$\mathbf{u}^k = \begin{pmatrix} \mathbf{u}_0^k \\ \cdot \\ \mathbf{u}_2^k \\ \cdot \end{pmatrix}, \quad \mathbf{u}^{k+1} = \begin{pmatrix} \cdot \\ \mathbf{u}_1^{k+1} \\ \cdot \\ \mathbf{u}_3^{k+1} \end{pmatrix}.$$

The term $\mathbf{F}\mathbf{u}^k$ is approximated by a sum of two components $\mathbf{F}_a(\mathbf{u}^{k+1} + \mathbf{u}^{k-1}) + \mathbf{F}_b\mathbf{u}^k$, where $\mathbf{F}_a$ and $\mathbf{F}_b$ are matrices depending on $\mathbf{F}$ such that $\mathbf{F}_a = \varsigma^{-1}(\mathbf{F} - \mathbf{F}_b)$, where $\varsigma = 2$. If the matrix $\mathbf{M} - \sigma\mathbf{F}_a$ is invertible[1], we can reformulate Eq. (5) as

$$\mathbf{u}^{k+1} = \mathbf{u}^{k-1} + (\mathbf{M} - \sigma\mathbf{F}_a)^{-1}\,\sigma\left(\mathbf{f}^k + 2\mathbf{F}_a\mathbf{u}^{k-1} + (\mathbf{F}_b - \mathbf{D})\mathbf{u}^k\right). \tag{6}$$

3.1. Conservation of energy.

Let $\mathbf{E}^k$ be $\sigma^{-1}\mathbf{M}(\mathbf{u}^{k+1} - \mathbf{u}^{k-1}) + \mathbf{D}\mathbf{u}^k - \mathbf{f}^k - \mathbf{F}\mathbf{u}^k$; see Eq. (5). We consider the equation $\left(\mathbf{u}^{k+1} + \mathbf{u}^{k-1}\right)^T \mathbf{E}^k + \left(\mathbf{E}^{k+1} + \mathbf{E}^{k-1}\right)^T \mathbf{u}^k = 0$. This can be expressed as

$$\left(\mathbf{u}^{k+1} + \mathbf{u}^{k-1}\right)^T \mathbf{f}^k + \left(\mathbf{f}^{k+1} + \mathbf{f}^{k-1}\right)^T \mathbf{u}^k + \left(\mathbf{u}^{k+1} + \mathbf{u}^{k-1}\right)^T \left(\mathbf{F} + \mathbf{F}^T\right)\mathbf{u}^k = \frac{P^{k+1} - P^{k-1}}{\sigma},$$

where the terms

$$P^k = (\mathbf{u}^k)^T\mathbf{M}\mathbf{u}^k + (\mathbf{u}^{k+1})^T\mathbf{M}\mathbf{u}^{k-1} \tag{7}$$

represent discrete energy at instance k. For zero source terms $\mathbf{f}^k = 0$ and $\mathbf{F} = 0$, we have $P^{k+1} = P^{k-1}$; that is, perfect conservation of energy.

The stability of the time integration is guaranteed if the components in Eq. (7) are bounded. Thus, we require a lower bound for $(\mathbf{u}^{k+1})^T\mathbf{M}\mathbf{u}^{k-1}$. To achieve

[1]Since $\mathbf{M} - \sigma\mathbf{F}_a$ is a diagonal and positive definite matrix, the inverse is diagonal and the iteration process is highly efficient.

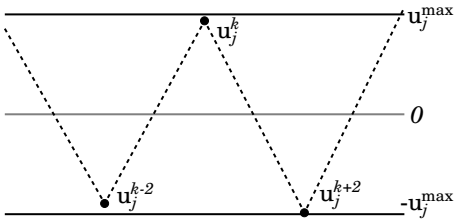

FIGURE 3. Stability is obtained by avoiding variables to change signs on consequent instances.

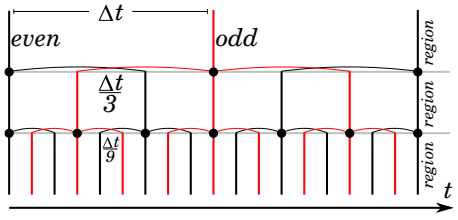

FIGURE 4. Even (black) and odd (red) time instances always match when regional time step sizes are set as $\frac{\Delta t}{3^i}$.

this, one usually employs the so-called Courant-Friedrichs-Lewy (CFL) condition [38, 30, 10]. By assuming $\mathbf{f}^k = 0$ in Eq. (5), we can write

$$2\mathbf{u}^k - \mathbf{u}^{k-2} - \mathbf{u}^{k+2} = \mathbf{M}^{-1}\sigma\left(\mathbf{D}-\mathbf{F}\right)\left(\mathbf{u}^{k+1} + \mathbf{u}^{k-1}\right) = \mathbf{M}^{-1}\sigma\left(\mathbf{D}-\mathbf{F}\right)\mathbf{M}^{-1}\sigma\left(\mathbf{F}-\mathbf{D}\right)\mathbf{u}^k.$$

In addition, we have

$$\frac{(\mathbf{u}^k)^T(2\mathbf{u}^k - \mathbf{u}^{k-2} - \mathbf{u}^{k+2})}{(\mathbf{u}^k)^T\mathbf{u}^k} = \frac{(\mathbf{u}^k)^T\mathbf{M}^{-1}(\mathbf{D}-\mathbf{F})\mathbf{M}^{-1}(\mathbf{F}-\mathbf{D})\mathbf{u}^k}{(\mathbf{u}^k)^T\mathbf{u}^k}\sigma^2 \leq \chi_{\max}\sigma^2 \leq 4\chi_{\max}\Delta t^2,$$

where $\chi_{\max}$ is the largest eigenvalue of the system matrix $\mathbf{M}^{-1}(\mathbf{D}-\mathbf{F})\mathbf{M}^{-1}(\mathbf{F}-\mathbf{D})$. The left-hand side is bounded above by constant $C \leq 4$; that is, stability is obtained, if $\Delta t \leq \sqrt{C/4\chi_{\max}}$.

3.2. **Local time stepping.** According to the CFL condition, the smallest elements of the spatial grid specify the largest possible Δt, resulting in stable time integration. If the spatial tiling is locally refined, the usage of a globally uniform (global) time step size throughout the system can result in inefficient time integration. This motivates locally adaptive (local) time-stepping schemes.

We consider a simple central difference approach, where the global time step is divided into an odd number of local time steps [9, 52]. Our algorithms include an automated CFL kind of condition, which can be adapted to unstructured spatial discretizations. The method is an expansion of the leapfrog time-stepping strategy, and it does not require additional computational or memory resources. Alternative local time-stepping strategies can be found in the literature [23, 13, 17].

For stability, we want $\left|2\mathbf{u}_j^k - \mathbf{u}_j^{k-2} - \mathbf{u}_j^{k+2}\right|$ to be bounded from above by $C\mathbf{u}_j^{\max}$, where $\mathbf{u}^{\max}$ is a vector whose components $\mathbf{u}_j^{\max}$ fulfill $|\mathbf{u}_j^k| \leq \mathbf{u}_j^{\max}$.

Let $|\mathbf{A}|$ denote a matrix whose entries are the absolute values of the corresponding entries of $\mathbf{A}$, and $|\mathbf{A}|_j$ is a row vector consisting of the jth row of $|\mathbf{A}|$. Let Δt_j be the time step size in the neighborhood of $\mathbf{u}_j^k$. Without source terms, Eq. (5) combined with the triangle inequality and $\sigma \leq 2\Delta t$ leads to

$$\left|2\mathbf{u}_j^k - \mathbf{u}_j^{k-2} - \mathbf{u}_j^{k+2}\right| \leq 4\Delta t_j^2\left|\mathbf{M}^{-1}(\mathbf{D}-\mathbf{F})\mathbf{M}^{-1}(\mathbf{F}-\mathbf{D})\right|_j \mathbf{u}^{\max}.$$

The stability condition is satisfied if

$$\Delta t_j \leq \sqrt{\frac{C\mathbf{u}_j^{\max}}{4\left|\mathbf{M}^{-1}(\mathbf{D}-\mathbf{F})\mathbf{M}^{-1}(\mathbf{F}-\mathbf{D})\right|_j \mathbf{u}^{\max}}} \tag{8}$$

holds.

The choice of $\mathbf{u}^{\max}$ specifies how the condition is weighted between elements. For example, if the $\mathbf{u}^{\max}$ is the eigenvector corresponding to the maximal eigenvalue $\chi_{\max}$ of $\left|\mathbf{M}^{-1}(\mathbf{D}-\mathbf{F})\mathbf{M}^{-1}(\mathbf{F}-\mathbf{D})\right|$, then the global CFL criterion $\Delta t_j \leq \sqrt{C/4\chi_{\max}}$ is obtained. We choose the vector $\mathbf{u}^{\max}$ by assigning the same weight to each term in Eq. (7). Then, a diagonal matrix $\mathbf{M}$ implies $\mathbf{u}_j^{\max} = \mathbf{M}_{jj}^{-1/2}$.

We select σ in Eqs. (5) and (6) such that $\boldsymbol{\sigma}_{j,j} = 2\Delta t_j$. The local time-stepping technique is explicit, and the diagonality implies efficiency.

The interfaces between different time step sizes need to be considered carefully because the conservation of discrete energy, Eq. (7), is slightly violated. Our approach is to set a global maximal time step size Δt and divide that locally by $s_j = 3^i$, $i \in \mathbb{N}$, to obtain local time interval $\Delta t_j = \frac{\Delta t}{s_j}$. With this strategy, all the even and odd time instances with regions of larger time step size have matching even and odd instances on regions of smaller time interval, as illustrated in Fig. 4. This seems to maintain the system energy when integrated over longer time periods, as suggested by the numerical experiments in Sections 5.1 and 5.5.

4. Time-harmonic problems

In the previous sections, we considered wave propagation in the time domain. In the frequency domain, the source terms $\bar{f} = \mathbf{f}e^{\mathrm{i}\omega t}$ generate time-harmonic solutions $\bar{u} = \mathbf{u}e^{\mathrm{i}\omega t}$, where ω is the angular frequency. In this section, we show how the explicit time integration scheme of Eq. (6) can be imbedded into an iterative algorithm to solve time-harmonic problems. For problems with single angular frequency, we introduce a time integration scheme by employing $\sigma = \frac{2\sin\omega\Delta t}{\omega}$ in Eq. (5), and additionally, $\varsigma = 2\cos\omega\Delta t$ in Eq. (6). For local time stepping, we have diagonal matrices $\boldsymbol{\sigma}$ and $\boldsymbol{\varsigma}$ with elements $\boldsymbol{\sigma}_{j,j} = \frac{2\sin\omega\Delta t_j}{\omega}$ and $\boldsymbol{\varsigma}_{j,j} = 2\cos\omega\Delta t_j$. In addition, the consistency error is minimized by taking advantage of the a priori known properties of time-harmonic waves.

4.1. Efficient iteration methods.

It is known that the time-harmonic steady state is reached by integrating a time-dependent equation asymptotically in time (the asymptotic approach). This approach is a reasonable choice if the wave propagates without reflections or if it is reflected by a convex object. Otherwise, the convergence to the time-harmonic state can be slow. This is why we proceed by generalizing a technique pioneered by Bristeau, Glowinski, and Périaux [8] to discrete exterior calculus and linear wave equations.

This provides us with a controlled version of the asymptotic approach based on quadratic optimization within time period $\frac{2\pi}{\omega}$. By dividing the time period into T time steps, we see that for a time-harmonic solution, one has $\mathbf{u}^{k+T} - \mathbf{u}^k = 0$, where $\mathbf{u}^k$ is the solution at the kth time step and $\mathbf{u}^{k+T}$ is the solution at the $(k+T)$th time step (T is an even integer). Since $\mathbf{u}^{k+T}$ can be solved with respect to $\mathbf{u}^k$ from Eq. (6), we can present the problem as a minimization of the squared $\mathbf{M}$-norm $\|\mathbf{u}^{k+T} - \mathbf{u}^k\|_{\mathbf{M}}^2 = \|\mathbf{A}\mathbf{u}^k + \mathbf{b}\|_{\mathbf{M}}^2$, where $\mathbf{A}$ is a time integration matrix and

$\mathbf{b}$ represents the source terms and power transfer for a single time period. The minimization problem is equivalent to a linear system:

$$\hat{\mathbf{A}}^*\Lambda\hat{\mathbf{A}}\begin{pmatrix}\mathbf{u}^k\\ \mathbf{u}^{k+1}\end{pmatrix} = -\hat{\mathbf{A}}^*\Lambda\sum_{i=1}^{T/2}\left(\left(\prod_{(T-2i)/2}\mathbf{B}^{-1}\mathbf{C}\right)(\Lambda\mathbf{B})^{-1}\sigma\begin{pmatrix}\mathbf{f}^{2i-1}\\ \mathbf{f}^{2i}\end{pmatrix}\right), \tag{9}$$

where k is an even integer, $\hat{\mathbf{A}} = \prod_{T/2}(\mathbf{B}^{-1}\mathbf{C}) - \mathbf{I}$, $\hat{\mathbf{A}}^*$ is its adjoint operator (also known as backward time integration), $\Lambda = \mathrm{diag}(\mathbf{M}, \mathbf{M})$,

$$\mathbf{B} = \mathbf{I} + \Lambda^{-1}\sigma\begin{pmatrix}\varsigma^{-1}(\mathbf{F}_b - \mathbf{F}) & \mathbf{0}\\ (\mathbf{D} - \mathbf{F}_b) & \varsigma^{-1}(\mathbf{F}_b - \mathbf{F})\end{pmatrix},$$
$$\mathbf{C} = \mathbf{I} + \Lambda^{-1}\sigma\begin{pmatrix}\varsigma^{-1}(\mathbf{F} - \mathbf{F}_b) & -(\mathbf{D} - \mathbf{F}_b)\\ \mathbf{0} & \varsigma^{-1}(\mathbf{F} - \mathbf{F}_b)\end{pmatrix},$$

and $\mathbf{I}$ is the identity matrix.

Since Eq. (9) has a symmetric and positive definite coefficient matrix $\hat{\mathbf{A}}^*\Lambda\hat{\mathbf{A}}$, we use the conjugate gradient method for the solution process. To compute the gradient by the adjoint equation technique, each conjugate gradient iteration step requires integration over one time period with operator $\hat{\mathbf{A}}$ and integration over one time period with the adjoint operator $\hat{\mathbf{A}}^*$. The computational cost of these time integrations is about the same. The conjugate gradient iteration is computationally twice as demanding as integration from $\mathbf{u}^k$ to $\mathbf{u}^{k+T}$.

Another alternative to construct a quadratic optimization problem for time-harmonic solutions is to consider half of the time period. In this case, $\|\mathbf{u}^{k+T/2} + \mathbf{u}^k\|^2_{\mathbf{M}}$ should be minimized, as shown in Chapter 9 [31]. Only the first half of the time period is used, and the computational cost of a conjugate gradient iteration is roughly the same as the computational cost of an asymptotic iteration.

We start the iteration from zero initial values; that is, $\mathbf{u}^0 = 0$. To get a smooth initial approximation, the source terms are not switched on abruptly at $t = 0$ but smoothly instead. For this, the right-hand side source terms $\bar{f}$ are multiplied by

$$w_{\mathrm{tr}} := \left(2 - \sin\left(\frac{\pi t}{2T_{\mathrm{tr}}}\right)\right)\sin\left(\frac{\pi t}{2T_{\mathrm{tr}}}\right)$$

during the transient period $0 \le t < T_{\mathrm{tr}}$. This technique is called the Mur transition [28]. In numerical experiments, we use a three-stage iteration method. First, the initial condition is computed by the Mur transition. Second, the asymptotic iteration is used, and third, the convergence is accelerated by the control realized by the conjugate gradient algorithm.

4.2. **Harmonic Hodge.** The discrete Hodge of Eq. (3) is built on the assumption of locally constant fields in the neighbourhood of the point where the material relation is imposed. In time-harmonic problems, however, it is possible to estimate a priori how the solution will vary in the vicinity of the point. Next, we derive such an approach to minimize the consistency error in time harmonic problems. This results in another discrete Hodge matrix, which we call **harmonic Hodge**.

The procedure to optimize the discrete Hodge for time-harmonic problems is a least square approach minimizing the following norm:

$$\|\star_p\bar{u}_p(j) - \bar{u}_{p*}(j)\|^2 ,$$

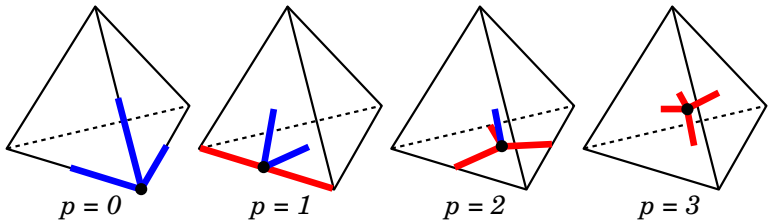

FIGURE 5. Sets $S(\partial c_j^p)$ and $S(c_j^p)$ of a node ($p = 0$), an edge ($p = 1$), a facet ($p = 2$), and a volume ($p = 3$). The edges of $S(\partial c_j^p)$ to the circumcenters of the bounding cells are shown in red, and the edges of $S(c_j^p)$ to the circumcenters of the neighboring $(p+1)$-cells are shown in blue.

where u is integrated in "all directions" over a unit n-sphere, $n = 1, 2, 3$. The minimum is when the derivative vanishes.

In terms of u and its complex conjugate u^*, the jth entry of the diagonal harmonic Hodge is

$$\star_p(j,j) = \frac{\int_\Omega (\mathbf{R}_\Omega u^*)_p(j)\,(\mathbf{R}_\Omega u)_{p*}(j)\,\mathrm{d}\Omega}{\int_\Omega (\mathbf{R}_\Omega u^*)_p(j)\,(\mathbf{R}_\Omega u)_p(j)\,\mathrm{d}\Omega}\,, \tag{10}$$

where Ω is a unit n-sphere and $\mathbf{R}_\Omega$ an operator that rotates u while integrating in all directions over Ω.

The time-harmonic solution of a wave at point $\mathbf{x}$ is of the form $u = e^{\mathbf{i}\boldsymbol{\kappa}\cdot\mathbf{x}}$, where $\boldsymbol{\kappa}$ is the vectorial wave number. Substituting this back to (10) yields

$$\star_p(j,j) = \frac{|c_j^{p*}|}{|c_j^p|}\left(1 + \sum_{e\in S(\partial c_j^p)} \frac{w_e\kappa^2 r_e^2}{4+2n} - \sum_{e\in S(c_j^p)} \frac{w_e\kappa^2 r_e^2}{4+2n}\right) + \mathcal{O}(\kappa^4 r^4)\,, \tag{11}$$

where n is the dimension of space, and the non-negative weights w_e are proportional volume terms, and hence they should fulfill condition

$$\sum_{e\in S(\partial c_j^p)\cup S(c_j^p)} w_e = 1.$$

The other terms in (11) are specified as follows: $S(\partial c_j^p)$ is the set of edges from the circumcenter of c_j^p to the circumcenters of the bounding cells of c_j^p, and $S(c_j^p)$ is the set of edges from the circumcenter of c_j^p to the circumcenters of the neighboring $(p+1)$-cells. Wave number κ is $\|\boldsymbol{\kappa}\|$, and r_e is the length of edge e (see Fig. 5).

For example, let us consider a two-dimensional triangular grid of edge length h. The primal cell volumes are $|c_j^0| = 1$, $|c_j^1| = h$, and $|c_j^2| = \frac{\sqrt{3}}{4}h^2$. By ignoring the boundary elements, the dual cell volumes are $|c_j^{0*}| = \frac{\sqrt{3}}{2}h^2$, $|c_j^{1*}| = \frac{1}{\sqrt{3}}h$, and $|c_j^{2*}| = 1$. The effective lengths are $r_e = \frac{h}{2}$ for $e \in S(c_j^0) \cup S(\partial c_j^1)$, $r_e = \frac{h}{\sqrt{12}}$ for $e \in S(c_j^1) \cup S(\partial c_j^2)$, and $r_e = 0$ otherwise. The terms of harmonic Hodge depend on the choice of the weights w_e. If the computation does not include discrete 2-forms, we recommend to set $w_e = 0$ for $e \in S(c_j^1) \cup S(\partial c_j^2)$. Then Eq. (11) indicates $\star_0(j,j) = \frac{\sqrt{3}}{2}h^2\left(1 - \frac{\kappa^2 h^2}{32}\right)$ and $\star_1(j,j) = \frac{1}{\sqrt{3}}\left(1 + \frac{\kappa^2 h^2}{32}\right)$. However, if the

computation ignores 0-forms, we recommend setting $w_e = 0$ for $e \in S(c_j^0) \cup S(\partial c_j^1)$. This indicates $\star_1(j,j) = \frac{1}{\sqrt{3}}\left(1 - \frac{\kappa^2 h^2}{96}\right)$ and $\star_2(j,j) = \frac{4}{\sqrt{3}h^2}\left(1 + \frac{\kappa^2 h^2}{96}\right)$.

5. Numerical experiments

Next, the presented framework is applied to several branches of physics. We consider quantum mechanics in Section 5.1, linear acoustics in Section 5.3, and electromagnetics in Section 5.4. We also perform numerical experiments by coupling linear elasticity and linear acoustics in Section 5.5.

The numerical experiments demonstrate versatile finite difference simulations in structured and unstructured grids. Especially, the applications are designed to indicate the difference between the structured grids described in Section 2.1, and clarify the advantage of employing harmonic Hodge instead of general Hodge. They also consider the efficiency of a local time-stepping strategy in comparison to global time stepping by examining the conservation of energy and the computational costs.

The described algorithms are implemented in C++ programming language, and the parallelization is applied with a message passing interface (MPI). Similarly to other finite difference approaches, the particular implementation parallelizes almost perfectly, as our previous studies suggest [33].

5.1. **Long-term stability.** The full system of Eq. (1), where F = 0, can be expressed as

$$\begin{pmatrix}
\frac{\partial_t}{c} & \partial_x & \partial_y & \partial_z & 0 & 0 & 0 & 0 \\
\partial_x & \frac{\partial_t}{c} & 0 & 0 & 0 & \partial_z & -\partial_y & 0 \\
\partial_y & 0 & \frac{\partial_t}{c} & 0 & -\partial_z & 0 & \partial_x & 0 \\
\partial_z & 0 & 0 & \frac{\partial_t}{c} & \partial_y & -\partial_x & 0 & 0 \\
0 & 0 & -\partial_z & \partial_y & \frac{\partial_t}{c} & 0 & 0 & -\partial_x \\
0 & \partial_z & 0 & -\partial_x & 0 & \frac{\partial_t}{c} & 0 & -\partial_y \\
0 & -\partial_y & \partial_x & 0 & 0 & 0 & \frac{\partial_t}{c} & -\partial_z \\
0 & 0 & 0 & 0 & -\partial_x & -\partial_y & -\partial_z & \frac{\partial_t}{c}
\end{pmatrix}
\begin{pmatrix} u_0 \\ u_{1x} \\ u_{1y} \\ u_{1z} \\ u_{2x} \\ u_{2y} \\ u_{2z} \\ u_3 \end{pmatrix}
=
\begin{pmatrix} f_0 \\ f_{1x} \\ f_{1y} \\ f_{1z} \\ f_{2x} \\ f_{2y} \\ f_{2z} \\ f_3 \end{pmatrix},$$

where c is the wave speed. One can easily see that the following always holds for complex variables:

$$\begin{pmatrix}
\frac{\partial_t}{c} & 0 & \partial_z & \partial_x - \mathrm{i}\partial_y \\
0 & \frac{\partial_t}{c} & \partial_x + \mathrm{i}\partial_y & -\partial_z \\
\partial_z & \partial_x - \mathrm{i}\partial_y & \frac{\partial_t}{c} & 0 \\
\partial_x + \mathrm{i}\partial_y & -\partial_z & 0 & \frac{\partial_t}{c}
\end{pmatrix}
\begin{pmatrix} u_0 + \mathrm{i}u_{2z} \\ \mathrm{i}u_{2x} - u_{2y} \\ u_{1z} - \mathrm{i}u_3 \\ \mathrm{i}u_{1y} + u_{1x} \end{pmatrix}
=
\begin{pmatrix} f_0 + \mathrm{i}f_{2z} \\ \mathrm{i}f_{2x} - f_{2y} \\ f_{1z} - \mathrm{i}f_3 \\ \mathrm{i}f_{1y} + f_{1x} \end{pmatrix}.$$

We consider the vector on the left-hand side as complex valued wave function ψ, the Weyl spinors. The obtained Weyl equation with a source term is

$$\left(\mathrm{I}_4 \frac{\partial_t}{c} + \sum_{\mu=x,y,z} \begin{pmatrix} 0 & \sigma_\mu \\ \sigma_\mu & 0 \end{pmatrix} \partial_\mu \right) \psi = f. \tag{12}$$

Here σ_x, σ_y, and σ_z are the Pauli matrices. In quantum mechanics, this relativistic wave equation describes massless spin-1/2 particles.

In this section, we examine the conservation of $u^*\mathrm{M}u$. As an example, we solve the Weyl equation in a sphere of radius $R = 2$. The mesh was generated by first introducing a structured two-dimensional grid on the boundary and inserting 30,113 randomly positioned nodes inside the sphere. Any two nodes were not allowed to

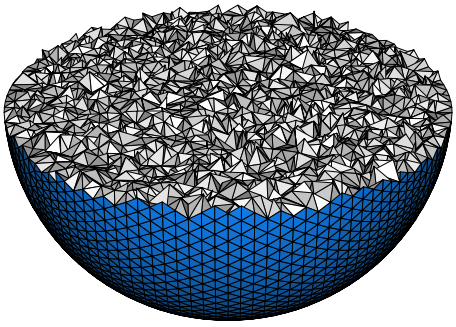

FIGURE 6. Illustration of the lower half of the random mesh.

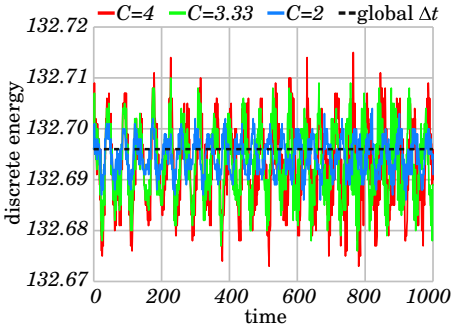

FIGURE 7. Conservation of energy with the local time-stepping technique employing $C = 4$, $C = 3.33$, and $C = 2$. Exact energy conservation is detected by global time stepping with $C = 4$.

be closer than 0.01 away from each other. The resulting unstructured mesh is illustrated in Fig. 6, and the element sizes are listed in Table 3.

	min	mean	max
primal length	0.010	0.13	0.31
dual length	4.2e-07	0.043	0.22
primal area	4.9e-05	0.0061	0.031
dual area	1.0e-11	0.0037	0.031
primal volume	2.2e-07	0.00015	0.0015
dual volume	8.2e-05	0.00097	0.0037

TABLE 3. Minimal, mean, and maximal element sizes in the unstructured mesh.

At $t = 0$, we initialize $u_0 = u_{1x} = u_{1y} = u_{1z} = u_{2x} = u_{2y} = u_{2z} = u_3 = \sin(2\pi R)$. We employ the general discrete Hodge given in Eq. (3) and integrate in time without any harmonic correction. The time integration is processed throughout $t \in [0, 1000]$ employing global and local time-stepping strategies. The stability limits were examined using Eq. (8) with different constants C. In the global time stepping, the smallest local time step is applied in the whole domain. We solve Eq. (12) with $\bar{f} = 0$ and specify the discrete energy with Eq. (7).

As illustrated in Fig. 7, the results indicate that the energy conservation holds with global time stepping, where the stability constant $C = 4$ is applied. The stability limit is relatively strict, since we observed immediate dispersion already with constant $C = 4.5$. The local time-stepping produces a small variation of energy, but we observe the long-term energy conservation. With stability constants

$C = 4$, $C = 3.33$, and $C = 2$, the standard deviations (SD) of energy are 0.0080, 0.0067, and 0.0033, respectively. These are small measures in comparison with the average energy level of 132.696.

The simulations were performed with 24 Intel (Xeon) Haswell (E5-2690v3, 64bits) cores. With local time stepping, the iteration times per period $T = 1$ were 0.958, 1.02, and 1.31 seconds with $C = 4$, $C = 3.33$, and $C = 2$, respectively. In contrast, the iteration time was 10.3 seconds with global time stepping with $C = 4$. Thus, we observed significant improvement in efficiency by employing local instead of global time stepping. In further experiments, the stability constant $C = 3.33$ is employed, if not mentioned otherwise.

5.2. **Wave speed error.** An error in wave speed generates cumulative phase error into the discrete solution. This error dominates especially when the domain diameter is large compared to the wavelength. In this section, we examine the error in wave propagation speed with different Hodge approximations and structured grids. The prototype problem is

$$\begin{aligned} \partial_t(\star_p \mathbf{m}_p \bar{u}_p) - \mathbf{d}_p^T \star_{p+1} \bar{u}_{p+1} &= \bar{f}_p + \mathbf{F}_p \bar{u}_p, \\ \partial_t(\star_{p+1} \mathbf{m}_{p+1} \bar{u}_{p+1}) + \star_{p+1} \mathbf{d}_p \bar{u}_p &= \bar{f}_{p+1} + \mathbf{F}_{p+1} \bar{u}_{p+1}, \end{aligned} \tag{13}$$

where p is chosen between 0 and $n-1$, and $n = 1, 2, 3$ is the dimension of the domain.

An n-dimensional domain, $n = 1, 2, 3$, illustrated in Fig. 8, is discretized with various structured grids, as described in Section 2.1. Each grid is cut by an n-sphere of radius 3, and an absorbing boundary condition is introduced at the mesh boundary $r = 3$. In region $2 < r < 3$, a matched layer is determined with absorption terms $\mathbf{F}_{p,j,j} = -3(r_j - 2)\star_p(j, j)$, where r_j is the radius at the center position of cell c_j^p. The source terms $\bar{f}_p$ and $\bar{f}_{p+1}$ are designed to generate a plane wave inside the domain. The matrices $\mathbf{m}_p$ and $\mathbf{m}_{p+1}$ are identity matrices. The reference solution is a harmonic plane wave $u = u_0 e^{\mathrm{i}\omega(t-x)}$, where $\omega = 2\pi$ is the angular frequency and t and x are the time and the propagated spatial distance, respectively. The wave propagation speed is $c = 1$ implying wavenumber $\kappa = \omega/c = 2\pi$, wavelength $\ell = 2\pi/\kappa = 1$, and frequency $\mathfrak{f} = c/\ell = 1$. Each simulation is carried out by 10 periods of Mur transition and 40 periods of asymptotic iteration. At the end of the simulations, we compare the numerical and the reference solutions inside a region $r < 1$ and adapt a linear regression curve indicating phase difference as a function of propagated spatial distance. The relative wave speed error is determined by the slope of the regression line.

In one dimension, the mesh is a combination of uniform line segments on the x-axis, and the length of segments is varied between $\frac{1}{200}$ and $\frac{1}{7}$. For comparison, the general Hodge of Eq. (3) and the harmonic Hodge of Eq. (11) with angular wavenumber $\kappa_k = 2\pi$ are applied. The simulated wave speed is found to be slower than expected (see Fig. 9). The wave speed error is proportional to h^2 and h^4 with general and harmonic Hodge, respectively. The polynomial approximation for harmonic Hodge improves the accuracy as the edge length decreases.

In two dimensions, there are two instances for the wave equation in Eq. (13). That is, $p = 0$ corresponding with discrete 0- and 1-forms, and $p = 1$ corresponding with discrete 1- and 2-forms. We examine four grid types, namely square, snub square, triangle, and tetrille. To compare the computational costs, we scale the grids to include 300 unknowns per unit area. This means that the edge length

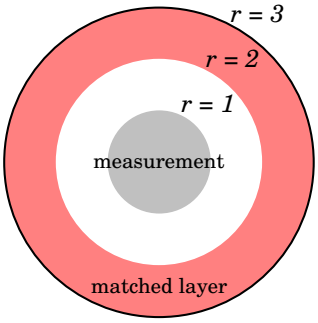

FIGURE 8. Two-dimensional illustration of the geometry.

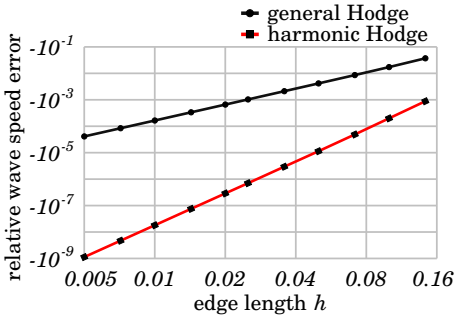

FIGURE 9. Wave speed error of one-dimensional wave Eq. (13).

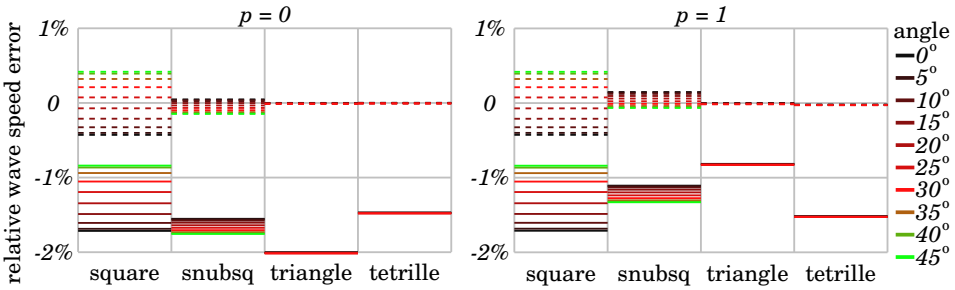

FIGURE 10. Wave speed error of two-dimensional wave Eq. (13), where $p = 0$ on the left and $p = 1$ on the right. The wave propagation angle is varied by 5 degree increments. The solid line represents error for general Hodge, and the dotted line represents error for harmonic Hodge.

of the square grid is $\frac{1}{10}$, and the scale of other grids depend on p. The wave propagation speed is studied as the propagation angles are increased in five degree increments. Since the grids are symmetric in several propagation directions (see Section 2.1), we restrict our numerical experiments to 10 propagation directions with square and snub square grids and 7 propagation directions with triangle and tetrille grids.

The relative wave speed errors are presented in Fig. 10. The general Hodge produces on average 1.4% slower wave propagation speed than expected. The smallest (0.82%) and the largest (2.0%) absolute values of wave speed errors are obtained with a triangle grid, for $p = 1$ and $p = 0$, respectively. The harmonic Hodge decreases absolute value of the wave speed error on average to 0.007%, but the angular dependency remains. The largest angular dependency, with a standard deviation of 0.33%, is obtained with square grid, which produces identical results for $p = 0$ and $p = 1$. The smallest angular dependencies (SD $< 0.01\%$) are obtained with tetrille and triangle grids.

In three dimensions, the wave Eq. (13) includes three instances with $p = 0, 1, 2$. The five structured grid types of Fig. 2 are employed to fill the spherical domain.

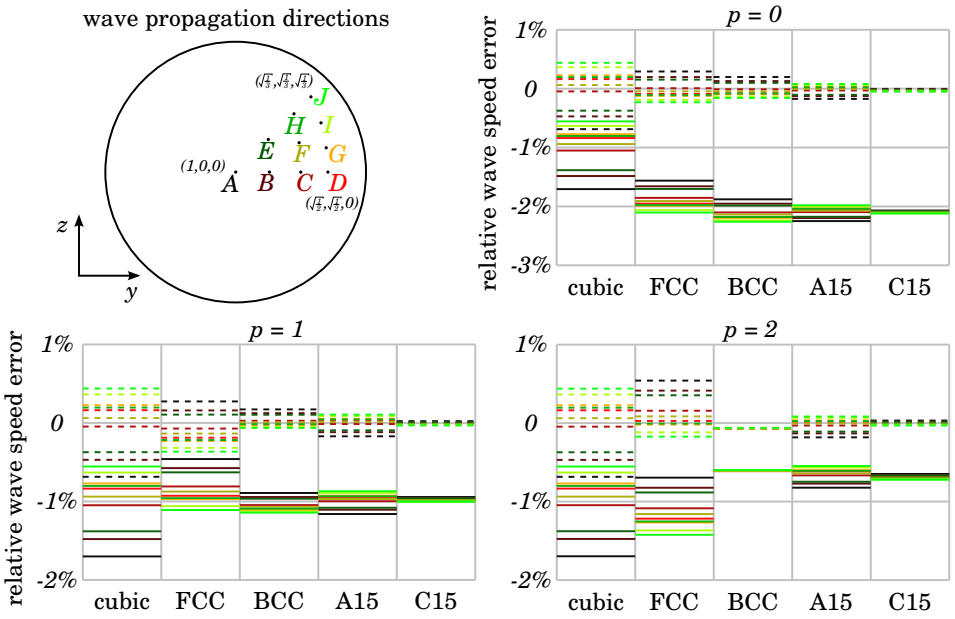

FIGURE 11. Wave speed error of three-dimensional wave Eq. (13) in 10 propagation directions. The solid line represents error for general Hodge, and the dotted line represents error for harmonic Hodge.

The grids are scaled to match the edge length $\frac{1}{10}$ of the cubic grid. That includes 4,000, 6,000 and 4,000 unknowns per unit volume for p values 0, 1, and 2, respectively. The wave speed is measured in 10 wave propagation directions, presented in the top-left corner of Fig. 11. Due to symmetries, these directions pierce the unit sphere at intervals of about 15 degrees.

The relative wave propagation speed errors are presented in Fig. 11. With the general Hodge, the wave speed is on average 1.2% shorter than expected. The smallest (0.6–0.7%) and largest (2.1%) absolute average errors are obtained with $p = 2$ and $p = 0$, respectively, when tetrahedral grids BCC, A15, and C15 were employed. In the case of $p = 1$, the smallest value 0.84% is obtained with the FCC structure. The harmonic Hodge nearly eliminates the systematic wave speed error and produces a propagation speed that is 0.012% too slow on average. The largest directional dependency, with a standard deviation of 0.38%, is observed with the cubic grid, independently of p. The C15 consistently produces the lowest standard deviation (SD $<$ 0.021% for every p). Other relatively isotropic structures are A15 (SD $<$ 0.093% for all p) and BCC (SD $<$ 0.13% for every p and especially 0.0046% for $p = 2$).

5.3. **Sound propagation.** In this section, we consider the numerical solution of sound propagation with both Hodge approximations of Eqs. (3) and (11) and different grids. We concentrate on the pollution effect, which is a phase error that deteriorates the accuracy of numerical solutions with high frequency. The effect has been studied in several papers in the finite element context (see, e.g., [3, 22, 2]). The techniques reducing the pollution effect include higher-order discretizations

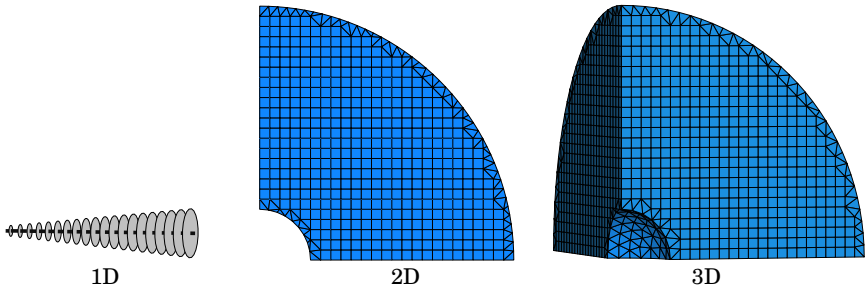

FIGURE 12. Illustration for one-, two-, and three-dimensional meshes with a Cartesian inner grid.

and optimal test functions [4, 15]. Presumably, minimization of the wave propagation speed error also decreases the pollution effect. That is, the harmonic Hodge, derived in Section 4.2 and verified in Section 5.2, is a good candidate to eliminate the pollution error. The number of mesh elements per wavelength is kept constant.

Sound propagation is modeled by the first order system of the acoustic wave equation as

$$\begin{aligned} \partial_t K^{-1} p + \operatorname{div} v &= 0, && \text{(Hooke's law)} \\ \partial_t \rho v + \operatorname{grad} p &= 0, && \text{(Newton's law)} \end{aligned} \tag{14}$$

where p is the pressure, v is the velocity, ρ is the density, and K is the stiffness coefficient. At the discrete level, it is a special case of Eq. (13), in which the discrete 0-form $\bar{u}_0$ and discrete 1-form $\bar{u}_1$ are interpreted as pressure and velocity, respectively. The material parameters are presented by the diagonal matrices $\mathbf{m}_0 = K^{-1}\mathbf{I}$ and $\mathbf{m}_1 = \rho\mathbf{I}$, where $K = 1$ and $\rho = 1$. The exact solution of Eq. (14) in a spherical domain centered at the origin is

$$p = \frac{1}{r} e^{\mathrm{i}\omega(t-r)}, \qquad v = \left(\frac{1}{r} + \frac{1}{\mathrm{i}\omega r^2}\right) e^{\mathrm{i}\omega(t-r)}, \tag{15}$$

where r is the distance from the origin and v represents the radial component of velocity. To examine the error between the numerical solution and the reference solution, a spherical layer with an inner radius of 0.5 and an outer radius of 2.5 is used as the computational domain. In the center of the domain, a spherical sound emitter is modeled by boundary conditions satisfying the exact solution of Eq. (15) at $r = 0.5$, and an absorbing boundary condition is applied on the outer boundary.

We discretize the problem in one, two, and three dimensions employing mesh structures, as shown in Fig. 12. We vary the inner grid such that all the different structured grids shown in Section 2.1 are tested. Similarly to previous experiments, the grids are scaled to make the computational costs comparable. The harmonic steady state results are obtained with 5 periods of Mur transition proceeding with $20\mathfrak{f}$ periods of asymptotic iteration, where $\mathfrak{f}$ is the frequency.[2] The relative error is integrated over the whole domain by comparing the numerical results to the exact solution elementwise.

In one dimension, the edge lengths $h = \frac{1}{10}$, $h = \frac{1}{20}$, and $h = \frac{1}{40}$ are considered. Since we employ a one-dimensional grid to represent a three-dimensional cone, we

[2]Wave propagates 10 times the distance between inner and outer boundaries.

modify the Hodge approximations of Eqs. (3) and (11) to spherical coordinates by replacing dual volume $|c_j^{p*}|$ with $x_j^2|c_j^{p*}|$, where x_j is the x-coordinate of the circumcenter of the cell c_j^p.[3] The angular wavenumber is $\kappa_k = 2\pi\mathfrak{f}$. The relative error of the solution is presented as a function of frequency in Fig. 13. The error seems to be of the form $h^2(a + b\mathfrak{f})$, where a and b are case-dependent constants. The magnitude of the pollution effect is measured by b. We find that with the general Hodge, the pollution effect is of magnitude $b = 12 \pm 1$, while with the harmonic Hodge, the pollution effect seems to be $b = (3.6 \pm 0.4)h^2$. This confirms the assumption that the pollution effect correlates to the propagation speed error.

The two-dimensional cylindral symmetric domain is a 90 degree sector of a disc. In this case, the dual volume $|c_j^{p*}|$ in the Hodge approximations has to be replaced with $(x_j + y_j)|c_j^{p*}|$, where x_j and y_j are the circumcenter coordinates of the cell c_j^p. Due to the symmetries, the boundaries inside $0.5 < r < 2.5$ are made to realize the condition, where the normal component of the velocity is zero. The pollution effects for different grid structures and Hodge approximations are illustrated in Fig. 14. With general Hodge, the relative error increases rapidly when the frequency is increased. Applying a linear regression curve indicates that the pollution effect is of the magnitude $b = 11 \pm 2$. With harmonic Hodge, the pollution effect seems to be much smaller. The value of b is 2 and 0.6 for the square and the snub square tilings, respectively, and $b < 0.01$ with the triangle and the tetrille grids.

In three dimensions, we consider two approaches for linear acoustics obtained by setting $p = 0$ and $p = 2$ in Eq. (13). The latter approach operates with discrete 2- and 3-forms and corresponds to Eq. (14) when $\bar{u}_2$ and $\bar{u}_3$ are interpreted as velocity and negative pressure, respectively. The material laws are included in the diagonal matrices $\mathbf{m}_2 = \rho\mathbf{I}$ and $\mathbf{m}_3 = K^{-1}\mathbf{I}$.

The discretization covers one-eighth of a hollow sphere. On the boundaries inside $0.5 < r < 2.5$, the normal component of the velocity is set to zero. The resulting relative errors are illustrated in Fig. 15. A relatively heavy pollution effect is observed, when the general Hodge is applied. Almost independently of p, the pollution term for the cubic grid is $b = 7.2 \pm 0.4$. The highest ($b = 14 \pm 1$) and lowest ($b = 3.2 \pm 0.4$) pollution effects are obtained with tetrahedral grids when $p = 0$ and $p = 2$, respectively. With the harmonic Hodge, the smallest pollution effect is obtained with the C15 grid ($b < 0.01$). The A15 and the BCC grids also produce a relatively small pollution effect ($b = 0.12 \pm 0.02$) when $p = 2$. The highest value of b is obtained with the cubic grid ($b = 2.0 \pm 0.1$). It is also worth mentioning that for low frequencies, the cubic grid seems to produce the most accurate results, $a = 2.7 \pm 0.1$. In contrast, the tetrahedral grids yield $a = 5.7 \pm 0.3$ and $a = 13 \pm 2$ on $p = 0$ and $p = 2$, respectively.

The conclusion is that the pollution effect can be eliminated almost completely when high-quality structured grids are applied with harmonic Hodge approximation. We observed no remarkable pollution effect with the C15 grid when the free distance in the domain was scaled up to 32 wavelengths. In two dimensions, the triangle and the tetrille grids succeed in eliminating the pollution effect up to 128 wavelengths of free distance.

[3]The Hodge of the basis vectors in Cartesian and spherical coordinates is not the same.

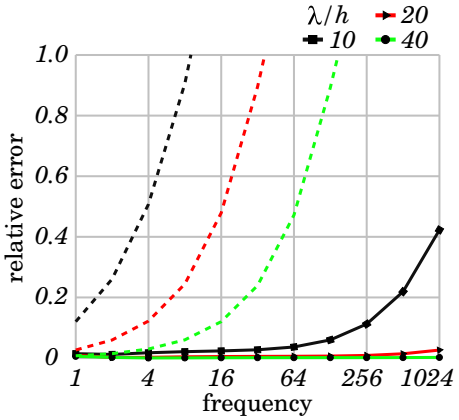

FIGURE 13. Relative error by frequency in one dimension.

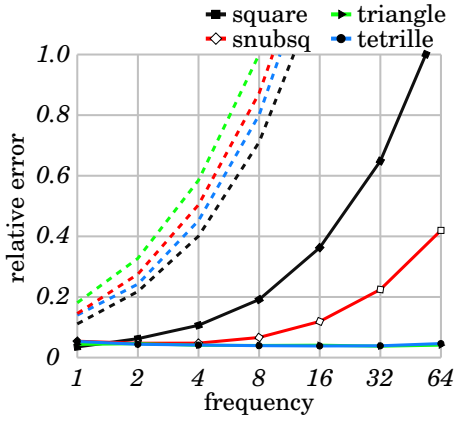

FIGURE 14. Relative error by frequency in two dimensions. The grids include 300 unknowns per ℓ^2.

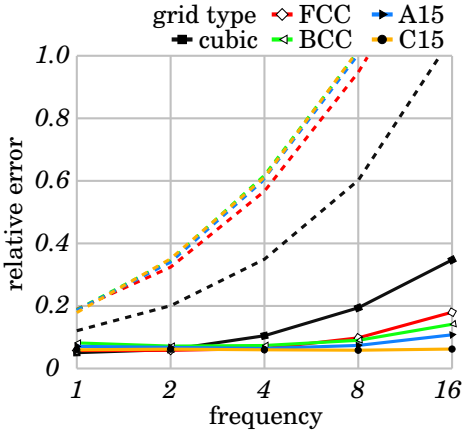

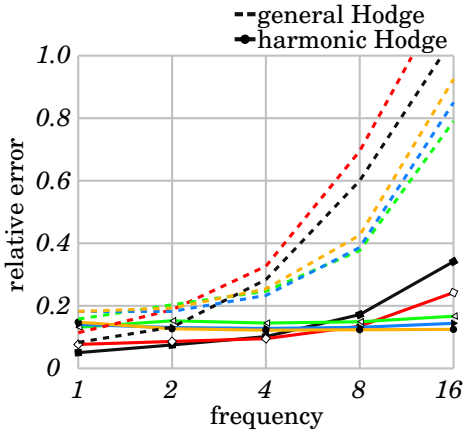

FIGURE 15. Relative error by frequency in three dimensions employing Eq. (13) with $p = 0$ (on the left) and $p = 2$ (on the right). The grids include 4,000 unknowns per ℓ^3.

5.4. **Electromagnetic scattering.** Electromagnetic waves satisfy

$$\partial_t \varepsilon e - \operatorname{curl} h = 0, \qquad \text{(Ampère's law)}$$
$$\partial_t \mu h + \operatorname{curl} e = 0. \qquad \text{(Faraday's law)}$$

The discrete counterpart of this is Eq. (13) with $p = 1$. Two alternative interpretations are possible. One may understand the 1-form $\bar{u}_1$ as the counterpart of the electric field and introduce $\mathbf{m}_1 = \varepsilon \mathbf{I}$ and $\mathbf{m}_2 = \mu \mathbf{I}$. Also, one may consider $\bar{u}_1$ as the magnetic field strength and introduce $\mathbf{m}_1 = \mu \mathbf{I}$ and $\mathbf{m}_2 = \varepsilon \mathbf{I}$.

Let us examine a scattering from 1,000 spherical particles packed into a spherical domain with a radius of 4.7898 and a packing density of 20%. The particle radius

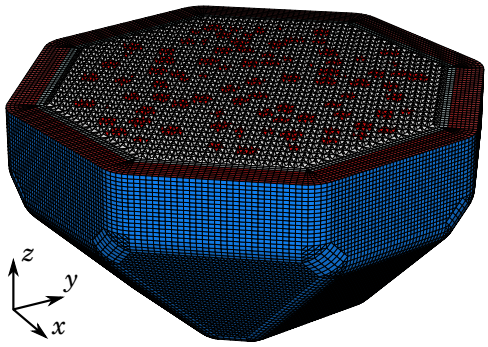

FIGURE 16. A convex structured grid with 26 intersecting planes employing the C15 grid with 6,000 unknowns per unit volume. Particles and the absorbing layer are marked by red.

is 0.28011, and the permittivity inside the particles is $\varepsilon = 2.25$. Elsewhere, permittivity is set to $\varepsilon = 1$. Permeability is $\mu = 1$ in the whole domain. The particle cluster is exposed by a plane wave with wavelength $\ell = 1$ propagating in directions $(0, 0, 1)$, $\sqrt{\frac{1}{2}}(1, 1, 0)$, and $-\sqrt{\frac{1}{3}}(1, 1, 1)$, as shown in Fig. 16.

We employ a convex structured mesh in the solution process. The mesh generation process, which is parallelized by MPI, intersects the desired grid by 26 planes and surrounds it by a layer, which is suitable for the demands of a 0.7 thick perfectly matched layer (PML). The particle positions are imported in element flags during the mesh-generation process.

The scattered wave is obtained by substracting the incident plane wave from the solution. The iteration process includes 5 periods of Mur transition, 60 periods of asymptotic iteration, and 30 control iterations. As a result, we obtain a near field solution on the inner interface of the PML. The far-field solution and the Muller matrices are computed using a near-to-far-field transformation presented in [45, 39]. To obtain the averaged Muller matrix, we solve the problem using two orthogonal linear polarizations. From the solutions, the averaged Muller matrix is calculated using 128 polarization planes for different angles ϕ.

We use the five three-dimensional grids shown in Fig. 2. In each case, we choose namely 10, 14, and 20 elements per wavelength. The discretization levels are scaled to include 6,000, 16,464, and 48,000 unknowns per unit volume. The reference result is computed with the C15 grid and harmonic Hodge. The reference task includes 50 elements per wavelength; that is, 750,000 unknowns per unit volume and 700 million unknowns in total. We compute two solutions by including the material variation on $\mathbf{m}_1$ and $\mathbf{m}_2$ and take the average of Muller matrices as the reference. The first components of the reference matrices are illustrated in Fig. 17. We denote a single orientation of averaged Muller matrix by S_i^{ref} and compute the relative Muller matrix error by

$$e = \sqrt{\frac{\int_0^\pi \sin\theta \sum_{i,j,k} \left(S_{i,j,k} - S_{i,j,k}^{\mathrm{ref}} \right)^2 d\theta}{\int_0^\pi \sin\theta \sum_{i,j,k} \left(S_{i,j,k}^{\mathrm{ref}} \right)^2 d\theta}}.$$

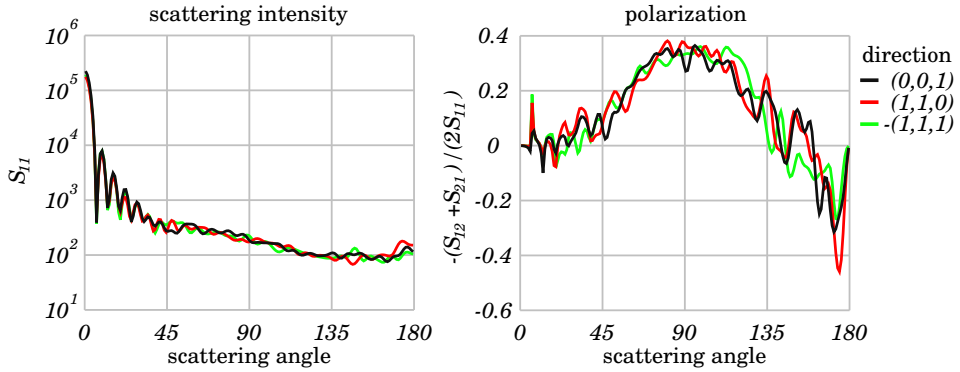

FIGURE 17. First components of averaged Muller matrices for three propagation directions.

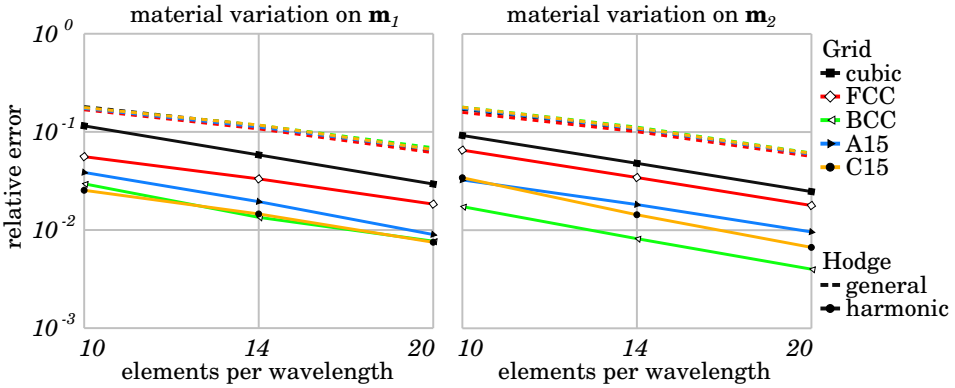

FIGURE 18. Relative error of Muller matrix by varying grid type, Hodge approximation, mesh element size, and the placement of material variation.

In both cases, the relative error is approximately 0.2%, indicating good accuracy.

The results in Fig. 18 demonstrate that the error decreases in relation to h^2. With the general Hodge approximation, the errors are relatively large, and no significant differences are observed between grid types. The smallest error is obtained with the FCC grid, and the error is about 7% smaller than the average of the errors obtained with other grids. The harmonic Hodge eliminates the systematic propagation speed error. The grid "anisotropy" becomes the most significant error source. The cubic and the FCC grids produce the largest errors. The BCC (surprisingly not the C15) seems to offer the best accuracy. It has possibly a better alignment for corresponding primal and dual elements.

Applying material variation on faces instead of edges seems to improve the averaged accuracy by a small margin. Particularly, the best accuracy is obtained by employing the BCC grid with a material variation on $\mathbf{m}_2$. One possible explanation is that $\mathbf{m}_2$ include more degrees of freedom than $\mathbf{m}_1$ because the number of faces is about 1.7 times larger than the number of edges on tetrahedral grids. Nevertheless, all the details of the results cannot be explained by this property. The fact

that the elements do not adapt particle surfaces may cause a loss of accuracy. For example, if the elements are larger than a distance between the particles, then the finite-dimensional model does not capture the problem to be modeled.

In conclusion, this numerical experiment indicates that the harmonic Hodge can certainly improve the simulation accuracy in comparison to the general Hodge, especially with tetrahedral meshes, where the error decreased to one-tenth. This means that the same accuracy is obtained for one-hundredth of the computational cost. If the domain size or the frequency increases, the difference of the two Hodge approximations is also expected to increase due to the pollution effect.

5.5. **A coupled problem of linear elasticity and acoustics.** The propagation of elastodynamic waves in isotropic media can be written by

$$\begin{aligned} \partial_t K^{-1} p + \operatorname{div} v &= 0, \\ \partial_t \rho v + \operatorname{grad} p + \operatorname{curl} w &= 0, \\ \partial_t \mu^{-1} w - \operatorname{curl} v &= 0, \end{aligned} \tag{16}$$

where $K = (\lambda + 2\mu)$ is the stiffness coefficient presented as functions of the Lamé parameters μ and λ, and ρ is the material density [26]. This is equivalent to the second-order elastodynamic wave equation $\rho \frac{\partial^2 u}{\partial t^2} - \operatorname{grad} K \operatorname{div} u + \operatorname{curl} \mu \operatorname{curl} u = 0$, where u is the displacement vector. The spatially discretized version of Eq. (16) is

$$\begin{aligned} \partial_t(\star_1 \mathbf{m}_1 \bar{u}_1) - \mathbf{d}_1^T \star_2 \bar{u}_2 &= \bar{f}_1 + \mathbf{F}_1 \bar{u}_1, \\ \partial_t(\star_2 \mathbf{m}_2 \bar{u}_2) + \star_2 \mathbf{d}_1 \bar{u}_1 - \mathbf{d}_2^T \star_3 \bar{u}_3 &= \bar{f}_2 + \mathbf{F}_2 \bar{u}_2, \\ \partial_t(\star_3 \mathbf{m}_3 \bar{u}_3) + \star_3 \mathbf{d}_2 \bar{u}_2 &= \bar{f}_3 + \mathbf{F}_3 \bar{u}_3, \end{aligned} \tag{17}$$

where the discrete forms $\bar{u}_1$, $\bar{u}_2$, and $\bar{u}_3$ represent the terms w, v, and $-p$, respectively. The material matrices are $\mathbf{m}_1 = \mu^{-1}\mathbf{I}$, $\mathbf{m}_2 = \rho\mathbf{I}$, and $\mathbf{m}_3 = K^{-1}\mathbf{I}$.

We solve the propagation of elastic waves in a standard three-dimensional object called the Stanford bunny [44]. The public domain surface mesh is first modified such that each surface 2-cell includes its circumcenter. The bunny is then scaled and positioned such that the length, width, and height are 3.11, 2.41, and 3.08, respectively, and the vertex positions $(x, y, z)^T$ belong to the intervals $x \in [-1.22, 1.89]$, $y \in [-1.24, 1.17]$, and $z \in [-0.33, 2.75]$. The surface mesh is embedded inside a cubic tiling, generated on interval $[-2.3, 2.9] \times [-2.3, 2.2] \times [-1.4, 3.8]$ with edge length $h = \frac{1}{20}$. The bottom of the bunny surface at $z < -0.2$ is attached to the ground by the boundary condition:

$$u_2 = \begin{cases} (z + 0.2)\sin(2\pi t)(1, 0, -1)^T, & t < 1, \\ 0, & t \geq 1. \end{cases}$$

The time time integration proceeds from $t = 0$ to $t = 200$.

We solve two different cases. First, we eliminate the external domain outside the bunny and consider elastic waves inside the object. The perfectly reflecting boundary condition, where $\bar{f}_p = 0$ and $\mathbf{F}_p = 0$, is applied on the surface at $z \geq -0.2$. The material parameters $\mu = 1$, $\rho = 1$, and $K = 4$ are employed. This implies that the longitudinal and the lateral waves propagate with wave speeds of 2 and 1, respectively. In Eq. (11), we have $\kappa_k = 2\pi$, $\kappa_k = 1.5\pi$, and $\kappa_k = \pi$ for $\star_1$, $\star_2$, and $\star_3$, respectively.

In the second case, a coupled acoustic wave equation is solved in the external domain outside the bunny. The acoustic problem is obtained by neglecting $\bar{u}_1$ from

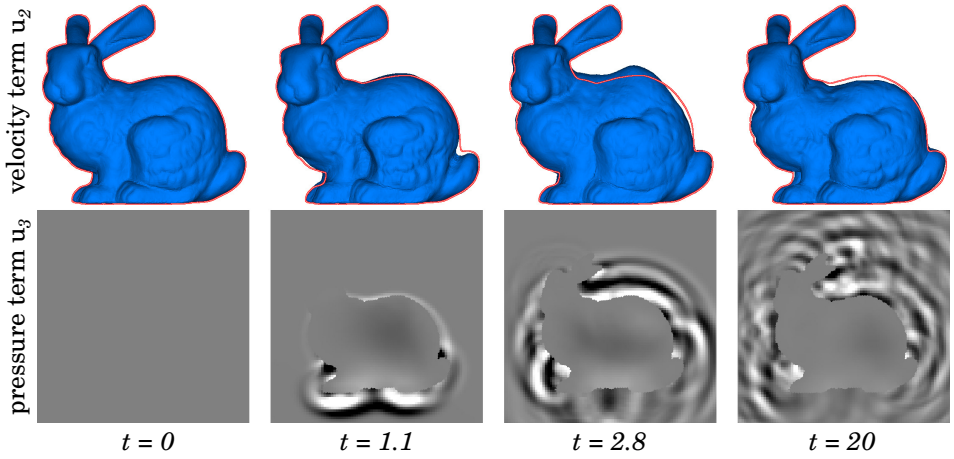

FIGURE 19. Velocity is illustrated by relocating vertex positions on the object surface by 2-form. The contours represent the zero velocity. A cross section of 3-form at $y = 0$ visualizes the pressure generated by elastic vibration.

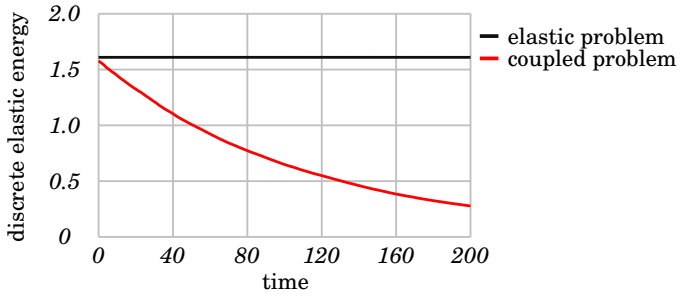

FIGURE 20. Conservation of energy.

the elastodynamic Eq. (17). On the interface, the continuity of the normal velocity is naturally imposed. On the acoustic part, the material parameters are $\rho = 0.01$ and $K = 0.0025$. This corresponds with an acoustic wave speed 0.5. Thus, $\kappa_j = 4\pi$ is selected for the discrete Hodge Eq. (11). To absorb the outgoing wave, we employ a PML with a thickness of 0.5 on the external boundary.

Figure 19 illustrates the time evolution of the coupled problem. The first longitudinal wave arrives on top of the bunny back at $t = 1.1$, and the first lateral wave reaches the top of the head at $t = 2.8$. The domain is filled with waves at $t = 20$.

The simulations are performed with a local time-stepping strategy on 24 Intel Haswell computing cores at 2.6 GHz. The evolution of discrete elastic energy, as given in Eq. (7), is illustrated in Fig. 20. In a purely elastic test, the elastic energy remains constant. The iteration time is 2.2 second for period $T = 1$. In contrast, that is 29 times faster than the iteration with a global time-stepping strategy, which evidently struggles with a few unstructured elements near the boundary. In the coupled problem, the elastic energy decreases exponentially due to the transformation into acoustic energy, which is absorbed into the PML. The iteration time is 5.6

seconds, which is 82 times faster than we observe with the global time-stepping strategy.

6. Conclusions

In this paper, we introduce a general class of linear wave propagation problems having a wide application area in classical and quantum physics. This class lends itself to so-called discrete exterior calculus and to generalized finite difference kinds of explicit solution schemes.

A key property of the finite-dimensional solution process is the precise fulfillment of conservation laws. Wave propagation problems incorporate two differential equations, and in both cases, the exterior derivate is imposed in the strong sense. For this reason, for instance, energy is also conserved in the finite-dimensional case. This is also demonstrated and verified by numerical experiments.

Finite difference methods usually include what is called a pollution effect. As the wave does not propagate with the same speed in all directions, the pollution effect increases the numerical error, especially when the problem is integrated over a long time interval. Our numerical experiments suggest, however, that the pollution effect can be practically eliminated by choosing an appropriate spatial grid consisting of regular blocks mimicking natural crystal structures and by adapting the discrete Hodge to the frequency on which the wave problem is fed. We use the term "harmonic Hodge" for such adapted matrices representing the Hodge operator in finite-dimensional spaces.

The numerical experiments in this paper cover linear acoustics, electromagnetism, coupled elasticity and acoustics, and the Weyl equation.

References

[1] F. Aurenhammer and R. Klein, *Voronoi diagrams*, Handbook of Computational Geometry (J.-R. Sack and J. Urrutia, eds.), North-Holland, Amsterdam, Netherlands, 2000, pp. 201–290.

[2] I. M. Babuska and S. A. Sauter, *Is the pollution effect of the FEM avoidable for the Helmholtz equation considering high wave numbers?*, Journal on Numerical Analysis **34** (1997), no. 6, 2392–2423.

[3] G. Bao, G. W. Wei, and S. Zhao, *Numerical solution of the Helmholtz equation with high wavenumbers*, International Journal for Numerical Methods in Engineering **59** (2004), no. 3, 389–408.

[4] H. Bériot, A. Prinn, and G. Gabard, *Efficient implementation of high-order finite elements for helmholtz problems*, International Journal for Numerical Methods in Engineering **106** (2016), no. 3, 213–240.

[5] A. Bossavit, *The Sommerville mesh in Yee-like schemes*, Scientific computing in electrical engineering: SCEE-2002 (Berlin), Mathematics in Industry, vol. 4, Springer, 2003, pp. 128–136.

[6] A. Bossavit and L. Kettunen, *Yee-like schemes on a tetrahedral mesh, with diagonal lumping*, International Journal of Numerical Modelling **12** (1999), no. 1–2, 129–142.

[7] ———, *Yee-like schemes on staggered cellular grids: A synthesis between FIT and FEM approaches*, IEEE Transactions on Magnetics **36** (2000), no. 4, 861–867.

[8] M. O. Bristeau, R. Glowinski, and J. Périaux, *Controllability methods for the computation of time-periodic solutions; Application to scattering*, Journal of Computational Physics **147** (1998), no. 2, 265–292.

[9] M. W. Chevalier, R. J. Luebbers, and V. P. Cable, *FDTD local grid with material traverse*, IEEE Transactions on Antennas and Propagation **45** (1997), no. 3, 411–421.

[10] M. Cinalli and A. Schiavoni, *A stable and consistent generalization of the FDTD technique to nonorthogonal unstructured grids*, IEEE Transactions on antennas and propagation **54** (2006), no. 5, 1503–1512.
[11] J. H. Conway, H. Burgiel, and C. Goodman-Strauss, *The symmetries of things*, CRC Press, 2016.
[12] J. H. Conway and N. J. A. Sloane, *Sphere packings, lattices and groups*, 3 ed., A series of comprehensive studies in mathematics, Springer, 1999.
[13] F. Coquel, Q. L. Nguyen, M. Postel, and Q. H. Tran, *Local time stepping applied to implicit-explicit methods for hyperbolic systems*, Multiscale Modeling & Simulation **8** (2010), no. 2, 540–570.
[14] B. N. Delaunay, *Sur la sphére vide*, Bulletin of Academy of Sciences of the USSR **7** (1934), 793–800.
[15] L. F. Demkowicz and J. Gopalakrishnan, *An overview of the discontinuous Petrov Galerkin method*, Recent Developments in Discontinuous Galerkin Finite Element Methods for Partial Differential Equations, Springer, 2014, pp. 149–180.
[16] M. Desbrun, E. Kanso, and Y. Tong, *Discrete differential forms for computational modeling*, Discrete Differential Geometry Oberwolfach Seminars **38** (2008), 287–324.
[17] J. Diaz and M. J. Grote, *Energy conserving explicit local time stepping for second-order wave equations*, SIAM Journal on Scientific Computing **31** (2009), no. 3, 1985–2014.
[18] Q. Du and D. Wang, *The optimal centroidal Voronoi tessellations and the Gersho's conjecture in the three-dimensional space*, Computers & Mathematics with Applications **49** (2005), no. 9–10, 1355–1373.
[19] D. Eppstein, J. M. Sullivan, and A. Üngör, *Tiling space and slabs with acute tetrahedra*, Computational Geometry: Theory and Applications **27** (2004), no. 3, 237–255.
[20] F. C. Frank and J. S. Kasper, *Complex alloy structures regarded as sphere packings. II. Analysis and classification of representative structures*, Acta Crystallographica **12** (1959), 483–499.
[21] A. N. Hirani, *Discrete exterior calculus*, Dissertation (Ph.D.), California Institute of Technology, 2003.
[22] F. Ihlenburg and I. Babuska, *Finite element solution of the Helmholtz equation with high wave number part ii*, Journal on Numerical Analysis **34** (1997), no. 1, 315–358.
[23] P. Joly, *Variational methods for time-dependent wave propagation problems*, Topics in computational wave propagation (2003), 201–264.
[24] J. Kepler, *Strena seu nive sexangula, 1611*, Clarendon Press, Oxford, UK, 1966, The Six-cornered Snowflake, (English translation by Colin Hardie).
[25] R. Kusner and J. M. Sullivan, *Comparing the Weaire-Phelan equal-volume foam to Kelvin's foam*, Forma **11** (1996), 233–242.
[26] L. D. Landau and E. M. Lifshitz, *Theory of elasticity*, Pergamon Press, Oxford, 1975.
[27] P. Maur, *Delaunay triangulation in 3D*, Tech. Report DCSE/TR-2002-02, University of West Bohemia in Pilsen, Department of Computer Science and Engineering, January 2002.
[28] G. Mur, *The finite-element modeling of three-dimensional electromagnetic fields using edge and nodal elements*, IEEE Transactions on Antennas and Propagation **41** (1993), no. 7, 948–953.
[29] R. Picard, *A structural observation for linear material laws in classical mathematical physics*, Mathematical Methods in the Applied Sciences **32** (2009), no. 14, 1768–1803.
[30] T. Weiland R. Schuhmann, *Stability of the FDTD algorithm on nonorthogonal grids related to the spatial interpolation scheme*, IEEE Transactions on magnetics **34** (1998), no. 5, 2751–2754.
[31] J. Räbinä, *On a numerical solution of the Maxwell equations by discrete exterior calculus*, Dissertation (Ph.D.), University of Jyväskylä, 2014.
[32] J. Räbinä, S. Mönkölä, and T. Rossi, *Efficient time integration of Maxwell's equations by generalized finite-differences*, SIAM Journal on Scientific Computing **37** (2015), B834–B854.
[33] J. Räbinä, S. Mönkölä, T. Rossi, A. Penttilä, J. Markkanen, and K. Muinonen, *Controlled time integration for the numerical simulation of meteor radar reflections*, Journal of Quantitative Spectroscopy and Radiative Transfer **178** (2016), 295–305.
[34] M. D. Sikiric, O. Delgado-Friedrichs, and M. Deza, *Space fullerenes: A computer search for new Frank-Kasper structures*, Acta Crystallographica Section A **66** (2010), no. 5, 602–615.

[35] A. Stern, Y. Tong, M. Desbrun, and J. E. Marsden, *Geometric computational electrodynamics with variational integrators and discrete differential forms*, Geometry, Mechanics, and Dynamics, Springer, 2015, pp. 437–475.

[36] J. M. Sullivan, *The geometry of bubbles and foams*, Foams and Emulsions (NATO ASI volume E) **354** (1998), 379–402.

[37] A. Taflove, *Application of the finite-difference time-domain method to sinusoidal steady state electromagnetic penetration problems*, IEEE Transactions on Electromagnetic Compatibility **22** (1980), no. 3, 191–202.

[38] A. Taflove and M. E. Brodwin, *Numerical solution of steady-state electromagnetic scattering problems using the time-dependent Maxwell's equations*, IEEE Transactions on Microwave Theory and Techniques **23** (1975), no. 8, 623–630.

[39] A. Taflove and K. Umashankar, *Radar cross section of general three-dimensional scatterers*, IEEE Transactions on Electromagnetic Compatibility **25** (1983), no. 4, 433–440.

[40] W. Thomson, *On the division of space with minimum partitional area*, Acta Mathematica **11** (1887), no. 1–4, 121–134.

[41] E. Tonti, *A direct formulation of field laws: The cell method*, Computer Modeling in Engineering & Sciences **2** (2001), no. 2, 237–258.

[42] E Tonti, *Why starting from differential equations for computational physics?*, Journal of Computational Physics **257** (2014), 1260–1290.

[43] E Tonti and F Zarantonello, *Algebraic formulation of elastodynamics: the cell method*, Computer Modeling in Engineering & Sciences(CMES) **64** (2010), no. 1, 37–70.

[44] G. Turk and M. Levoy, *Zippered polygon meshes from range images*, Proceedings of the 21st Annual Conference on Computer Graphics and Interactive Techniques (New York, NY, USA), SIGGRAPH '94, ACM, 1994, pp. 311–318.

[45] K. Umashankar and A. Taflove, *A novel method to analyse electromagnetic scattering of complex object*, IEEE Transactions on Electromagnetic Compatibility **24** (1982), no. 4, 397–405.

[46] E. VanderZee, A. N. Hirani, and D. Guoy, *Triangulation of simple 3D shapes with well-centered tetrahedra*, Proceedings of the 17th International Meshing Roundtable, 2008, pp. 19–35.

[47] G. F. Voronoi, *Nouvelles applications des paramétres continus á la théorie de formes quadratiques*, Journal für die reine und angewandte Mathematik **133** (1908), 97–178.

[48] D. Weaire and R. Phelan, *A counter-example to Kelvin's conjecture on minimal surfaces*, Philosophical Magazine Letters **69** (1994), no. 2, 107–110.

[49] T. Weiland, *A discretization method for the solution of Maxwell's equations for six-component fields*, Electronics and Communications AEUE **31** (1977), no. 3, 116–120.

[50] H. Whitney, *Geometric integration theory*, Princeton Univercity Press, Princeton, 1957.

[51] K. S. Yee, *Numerical solution of initial boundary value problems involving Maxwell's equations in isotropic media*, IEEE Transactions on antennas and propagation **14** (1966), no. 3, 302–307.

[52] S. S. Zivanovic, K. S. Yee, and K. K. Mei, *A subgridding method for the time-domain finite-difference method to solve Maxwell's equations*, IEEE Transactions on Microwave Theory and Techniques **39** (1991), no. 3, 471–479.

University of Jyvaskyla, Faculty of Information Technology, P.O. Box 35, FI-40014 University of Jyvaskyla, Finland

Current address: University of Helsinki, Department of Physics, P.O. Box 64, FI-00014 University of Helsinki, Finland

E-mail address: jukka.rabina@jyu.fi

University of Jyvaskyla, Faculty of Information Technology, P.O. Box 35, FI-40014 University of Jyvaskyla, Finland

E-mail address: lauri.y.o.kettunen@jyu.fi

University of Jyvaskyla, Faculty of Information Technology, P.O. Box 35, FI-40014 University of Jyvaskyla, Finland

E-mail address: sanna.monkola@jyu.fi

University of Jyvaskyla, Faculty of Information Technology, P.O. Box 35, FI-40014 University of Jyvaskyla, Finland

E-mail address: tuomo.j.rossi@jyu.fi